

Electronic charge transfer driven by spin cycloidal structure

Y. Ishii,^{1,*} S. Horio,² Y. Noda,² M. Hiraishi,¹ H. Okabe,¹ M. Miyazaki,³ S. Takeshita,¹ A. Koda,¹ K. M. Kojima,⁴ R. Kadono,¹ H. Sagayama,¹ H. Nakao,¹ Y. Murakami,¹ and H. Kimura²

¹*Institute of Materials Structure Science (IMSS),
High Energy Accelerator Research Organization (KEK), Tsukuba, Ibaraki 305-0801, Japan*

²*Institute of Multidisciplinary Research for Advanced Materials,
Tohoku University, Aoba Sendai 980-8577, Japan*

³*Graduate School of Engineering, Muroran Institute of Technology,
Muroran, Hokkaido 050-8585, Japan*

⁴*TRIUMF Centre for Molecular and Material Science
(TRIUMF-CMMS) and Quantum Matter Institute,
University of British Columbia, Vancouver, BC V6T 2A3, Canada*

Abstract

Muon spin rotation and resonant soft X-ray scattering experiments on prototype multiferroics RMn_2O_5 ($R = Y, Sm$) are used to demonstrate that the local electric displacements are driven by the spin-current (SC) mechanism. Small local electric displacements were evaluated by observing spin polarization at ligand O ions, for which implanted muons served as an extremely sensitive probe. Our results for YMn_2O_5 provide evidence that the spin polarization of O ions forming a spin cycloid chain with Mn spins increases in proportion to the vector spin chirality ($\mathbf{S}_i \times \mathbf{S}_j$) of the Mn ions. This relationship strongly indicates that the charge transfer between O and Mn ions is driven by the SC mechanism, which leads to the ferroelectricity accompanying O spin polarization.

I. INTRODUCTION

Manipulating the electronic state of materials by tuning their magnetic state is key to the development of new devices with multifunctional properties. To this end, multiferroic materials with coupling between magnetism and ferroelectricity provide promising playing grounds [1]. A number of studies on these multiferroics have prompted the development of theoretical models for the microscopic mechanism of magnetically driven ferroelectricity, such as the "spin-current" (SC) and "exchange-striction" (ES) models, in which a cycloidal spin chain and a collinear spin alignment, respectively, break the inversion symmetry [2–4].

Elucidating these local displacements associated with the electric polarization is critical for examining these models and gaining better understanding of multiferroics. However, previous attempts have achieved limited success because of the experimental difficulties associated with observing these local deviations, which are expected to be small in proportion to the electric polarization in most multiferroic materials. Recently, some authors have suggested that the charge transfer between transition-metal cations and oxygen ligands would represent the primary contribution to the ferroelectricity and that the charge transfer would also accompany oxygen spin polarization [5, 6]. Hence, resonant soft X-ray scattering (RSXS) experiments at the O K -edge were performed to observe the magnetic order of O ions for prototype multiferroic materials RMn_2O_5 and $RMnO_3$ ($R =$ rare earth) [7–12]. In particular, charge transfer was inferred to contribute to ferroelectricity in YMn_2O_5 and $Tb_{0.5}Gd_{0.5}Mn_2O_5$ on the basis of a one-to-one correspondence in the temperature and external magnetic field dependence, respectively, between the electric polarization and the magnetic scattering intensity of the O ions [8, 12]. Despite these efforts, RSXS measurements preclude quantitative discussion of the O spin polarization in evaluating the contribution of charge transfer to the ferroelectricity.

In the present paper, we report the extraction of information on the spin polarization of ligand O ions via a synergetic use of RSXS and muon spin rotation (μ SR) as mutually complementary techniques, as demonstrated for YMn_2O_5 . While the magnetic order associated with O spin polarization is inferred from the magnetic reflection of O $2p$ electrons via the O K edge RSXS, the magnitude of O spin polarization is estimated from the local magnetic field measured by μ SR; positive muons, which are regarded as pseudo-hydrogen atoms, exhibit a strong tendency to form OH bonds with oxygen ligands in nonmetallic

oxides, thus serving as a sensitive probe for spin polarization.

We use SmMn_2O_5 as a reference for comparison to YMn_2O_5 because they exhibit contrasting magnetic and ferroelectric properties as well as contrasting oxygen spin states [13–15]. Both of these materials undergo a sequence of dielectric and magnetic phase transitions. In the case of YMn_2O_5 , an incommensurate antiferromagnetic phase appears below 45 K. Electric polarization occurs upon cooling to 40 K, concomitant with a commensurate magnetic order (CM phase) with a magnetic propagation vector $\mathbf{q}_M = (1/2, 0, 1/4)$. With a further decrease in temperature to less than 18 K, the electric polarization rotates in the opposite direction, which is related to the transition to a low-temperature incommensurate magnetic (LT-ICM) phase. The magnetic structure has been clarified in previously reported neutron scattering experiments, where an approximately collinear magnetic alignment in the ab plane and spin cycloidal chain of Mn^{4+} moments along the c -axis were realized [16, 17]. This magnetic structure leads to the scenario that the ES model is responsible for the ferroelectricity in the CM phase, whereas the SC model is in effect for the LT-ICM phase [18]. By contrast, an incommensurate magnetic (ICM) phase appears below 34 K in SmMn_2O_5 . The electric polarization is enhanced upon the onset of a CM phase below 26 K with a perfect collinear magnetic structure with $\mathbf{q}_M = (1/2, 0, 0)$ [15, 19]. This magnetic structure suggests that the electric polarization in the CM phase is attributable to the ES model.

II. EXPERIMENT DETAILS

Single crystals of YMn_2O_5 and SmMn_2O_5 were grown by the PbO-PbF_2 flux method [20]. We performed RSXS experiments in which measurements at the O K -edge ($E \sim 530$ eV) were carried out at the BL-16A and BL-19B beamlines [21] at the Photon Factory, KEK, Japan. Conventional μSR experiments were performed at the M15 and M20 beamlines at TRIUMF, Canada. Zero-field (ZF) and transverse-field (TF) μSR were conducted using the LAMPF spectrometer and NuTime spectrometer.

III. RESULTS AND DISCUSSION

A. RSXS measurements

RSXS energy spectra around the O K -edge obtained for the CM phase of YMn_2O_5 and SmMn_2O_5 are shown in Fig. 1 (a), which reproduce those reported previously [8, 9, 11]. The incident X-rays were polarized perpendicular to the scattering plane (σ -polarized). In the spectrum of YMn_2O_5 , a well-defined peak is observed at $E \approx 530$ eV, which indicates the presence of spin polarization of O sites via charge transfer from Mn to O ions. By contrast, no such peak is observed in the spectra for SmMn_2O_5 , strongly suggesting the absence of the O spin polarization via Mn–O hybridization. Thus, we confirmed the oxygen ligands in the CM phase of YMn_2O_5 and SmMn_2O_5 have different electronic states. This conclusion is further supported by the azimuthal angle dependence of the intensity at $E = 530$ eV measured for YMn_2O_5 [see Fig. 1 (b)]. The resonant intensity increases as the azimuthal angle approaches $\psi = 90^\circ$. This observed angle dependence is in reasonable agreement with that calculated for the magnetic structure of O ions suggested by the present μSR experiment (see below).

B. Muon stopping sites

For the μSR measurement, we first narrowed down candidate sites for the interstitial muons in the RMn_2O_5 structure by investigating the Hartree potential obtained by first-principle calculations based on density functional theory (DFT). Fig. 2 (a) shows the crystal structure containing a unit cell in the paramagnetic phase of RMn_2O_5 . This structure has two independent sites for Mn (Mn^{4+} and Mn^{3+}) and four independent sites for O (sites O1 through O4). They form edge-sharing $\text{Mn}^{4+}\text{-O}_6$ octahedra running along the c -axis, whereas a pair of $\text{Mn}^{3+}\text{-O}_5$ pyramids links the $\text{Mn}^{4+}\text{-O}_6$ chains in the ab plane. The Hartree potential for this structure was calculated using the Vienna Ab initio Simulation Package (VASP) code [22] to explore the potential minima for a positive charge introduced by muons. Site1 and Site2 in Fig. 2 (a) correspond to the obtained local potential minima located near O2 and O4 sites, respectively.

These candidate sites were subsequently examined on the basis of the muon Knight shift data obtained by TF- μSR measurements under an external magnetic field ($H_c = 6$ T) applied

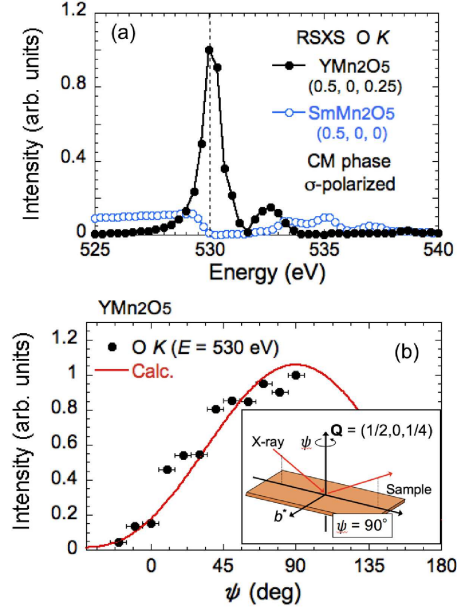


FIG. 1. (Color online). (a) Energy spectra of RSXS around the O K edge in RMn_2O_5 ($R = Y, Sm$). Each measurement was performed in the CM phase (26 K for YMn_2O_5 , 18 K for $SmMn_2O_5$) of each material. (b) Azimuth angle dependence of RSXS intensity at O K -edge ($E = 530$ eV) in YMn_2O_5 . The red curve represents the calculated values with the magnetic structure of O2 ions (shown in Fig. 4 (c)). The inset shows the scattering geometry at azimuthal angle $\psi = 90^\circ$. By definition, $\psi = 90^\circ$ indicates that the b^* -axis is perpendicular to the scattering plane.

along the c -axis. The frequency shift in the paramagnetic (PM) phase is determined by the local magnetic field (\mathbf{B}_{loc}) at the muon site, which is given by the vector sum of the dipolar fields generated by local magnetic moments:

$$\mathbf{B}_{loc} = \sum_j A_j^{\alpha\beta} \mu_j^\beta, \quad (1)$$

where the summation runs through the j -th Mn magnetic moment $\boldsymbol{\mu}_j = (\mu_j^x, \mu_j^y, \mu_j^z)$ located at $\mathbf{r}_j = (x_j, y_j, z_j)$ from a given muon site, $A_j^{\alpha\beta}$ is the corresponding dipole tensor (whose z -axis is chosen parallel with the crystalline c -axis), which is expressed by the equation

$$A_j^{\alpha\beta} = \frac{1}{r_j^3} \left(\frac{3\alpha_j\beta_j}{r_j^2} - \delta_{\alpha\beta} \right) \quad (\alpha, \beta = x, y, z). \quad (2)$$

Assuming that the Mn moments are aligned parallel to H_c in the PM phase, then

$$\mathbf{B}_{loc} = \frac{\chi_c}{N_A \mu_B} \sum_j A_j^{zz}, \quad (3)$$

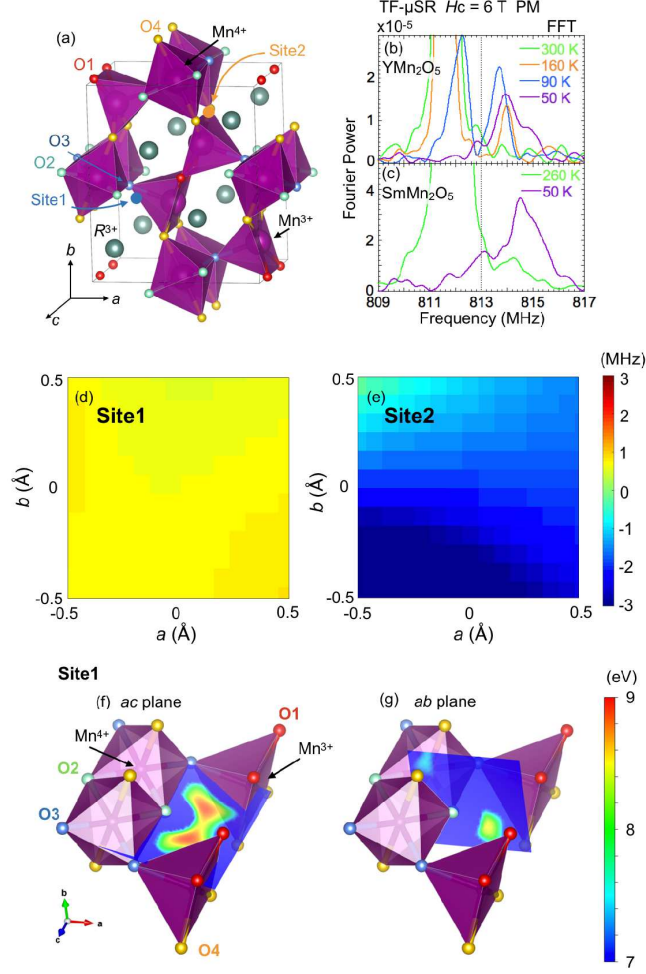


FIG. 2. (Color online) Fig. S1: (a) Crystal structure of RMn_2O_5 . Site1 and Site2 represent candidate muon stopping sites indicated by VASP calculations. (b)(c) FFT spectra of TF- μ SR at each temperature under an external magnetic field along the c -axis for YMn_2O_5 and $SmMn_2O_5$. The dashed line represents 813 MHz. (d)(e) Contour map of the local magnetic field (shown in terms of the frequency shift $\gamma_\mu \mathbf{B}_{loc}/2\pi$) in the ab plane around Site1 and Site2. Positive (negative) indicates parallel (antiparallel) to the external magnetic field. (f)(g) Hartree potential in the ac and ab planes around Site1.

where χ_c is the bulk magnetic susceptibility, N_A is Avogadro's number, and μ_B is the Bohr magneton.

Figures 2 (b)(c) show fast Fourier transforms (FFTs) of the TF- μ SR spectra in the PM phase ($T > 50$ K) of RMn_2O_5 , where the dashed line represents the null shift ($\gamma_\mu H_c/2\pi = 813$ MHz, where $\gamma_\mu/2\pi = 135.53$ MHz is the muon gyromagnetic ratio). A strong peak was

observed around 811.5 MHz at ambient temperature for both compounds. With decreasing temperature below ~ 160 K, an additional well-defined peak emerges at approximately 814 MHz, whereas the peak at 811.5 MHz diminishes and then disappears at ~ 50 K. It is inferred from these observations that there are two different muon stopping sites in the unit cell, where the \mathbf{B}_{loc} probed by muons is parallel or antiparallel to the direction of the external magnetic field, respectively. The intensity of Fourier power at 50 K decreases compared with that at ambient temperature, likely because of a strong relaxation near the Néel temperature.

These results were compared with the \mathbf{B}_{loc} calculated using Eq. (3) [23] for Site1 and Site2 in YMn_2O_5 . Figures 2 (d)(e) show the contour map of \mathbf{B}_{loc} in the ab plane around Site1 and Site2, where positive (negative) values represent \mathbf{B}_{loc} parallel (antiparallel) to the direction of an external field. Both the magnitude and sign of \mathbf{B}_{loc} for Site1 and Site2 are in good agreement with the experimental observations; thus, these two sites can be reasonably assigned as the most likely muon sites. This result further suggests that the muon occupancy is shifted from Site2 to Site1 as temperature decreases in the PM phase. A recent X-ray absorption spectroscopy (XAS) study of TbMn_2O_5 implies the occurrence of local buckling at the O4 site below $T \sim 180$ K in the PM phase, as evidenced by the thermal evolution of the pair-distribution function for a Tb–O bond [24]. The local buckling at the O4 site likely occurs also in YMn_2O_5 , where it causes a change of the local electrostatic potential around Site2, leading to a shift of muon occupancy from Site2 to Site1 at temperatures below $T \sim 160$ K. Figures 2 (f)(g) show the shape of the Hartree potential around Site1, as obtained by VASP calculations; this result suggests that the candidate area for the muon stopping site is broadened in the ac plane. Thus, we conducted ZF- μ SR for SmMn_2O_5 to further narrow the candidate muon sites.

C. ZF- μ SR measurements for SmMn_2O_5

Figure 3 (a) shows time spectra at 8 K (CM phase) with the initial muon spin polarization [$\mathbf{P}_\mu(t = 0)$] parallel to the c - and b -axes. The muon spin precession signal is clearly observed with $\mathbf{P}_\mu \parallel b$. The corresponding FFT spectrum in Fig. 3 (b) suggests two frequency components. The spectrum was subsequently analyzed by curve fitting [25]; the deduced frequencies are shown in Table I as B^{exp} . In sharp contrast, no precession is observed in the

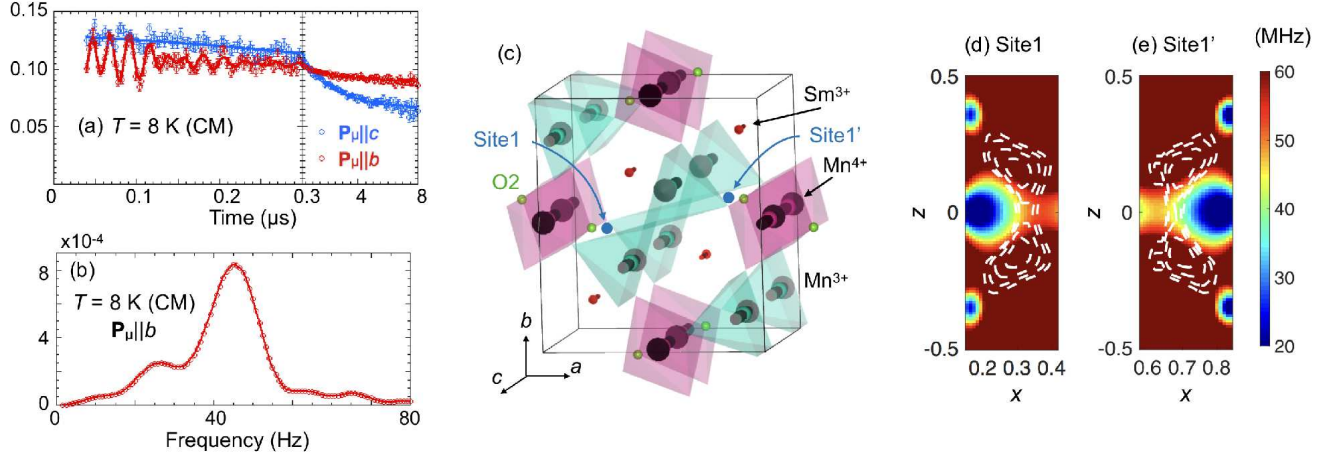


FIG. 3. (Color online) (a) Time spectra of ZF- μ SR for SmMn_2O_5 at 8 K in the CM phase, and (b) FFT of the time spectrum with $\mathbf{P}_\mu \parallel b$. (c) Magnetic structure in the CM phase of SmMn_2O_5 . Red and black arrows represent the magnetic moments of Sm and Mn ions, respectively. Site1^(\prime) correspond to muon stopping sites. (d)(e) Contour map of \mathbf{B}_{loc} in the ac plane around Site1 and Site1^(\prime). The magnitude is represented by the corresponding muon spin precession frequency ($\gamma_\mu \mathbf{B}_{\text{loc}}/2\pi$). Dashed lines represent the contour of the Hartree potential shown in Fig. 2 (f).

spectrum with $\mathbf{P}_\mu \parallel c$ within the experimental error. In addition, the curve fitting analysis failed to reproduce the spectrum. Because muon spin precession was induced by $\mathbf{B}_{\text{loc}} \perp \mathbf{P}_\mu$, these observations indicate that \mathbf{B}_{loc} at the relevant muon site is parallel to the c -axis. We calculated \mathbf{B}_{loc} for the magnetic structure of Sm and Mn ions shown in Fig. 3 (c) reported in the literature [15, 19]. In this magnetic structure, Site1 divides into two inequivalent sites, which we refer to as Site1 and Site1^(\prime). The calculated values of \mathbf{B}_{loc} around Site1 and Site1^(\prime) are shown in Figs. 3 (d)(e). Dashed lines in these figures represent the contour of the Hartree potential shown in Fig. 2 (f). In the area indicated by the VASP calculation, the sites where the calculated \mathbf{B}_{loc} are in good agreement with the experimental values are determined to be (0.301(1), 0.401(2), 0.00(1)) and (0.718(1), 0.599(2), 0.00(1)), respectively. The calculated \mathbf{B}_{loc} at these sites are also summarized in Table I as B^{calc} , which are in agreement with the experimental values. Here, we stress that B^{calc} reproduces B^{exp} without the assumption of spin polarization at the O sites, which is consistent with the results of the RSXS experiments [11].

TABLE I. Magnitude and direction of the local magnetic field (B_{loc}) at Site1⁽ⁱ⁾ in the CM phase in SmMn_2O_5 , where B^{exp} is deduced from ZF- μSR experiments and B^{calc} are calculated values. The magnitude is represented by the corresponding muon spin precession frequency ($\gamma_{\mu}B_{\text{loc}}/2\pi$).

Site	B^{exp} (MHz)	$B_{\text{dir}}^{\text{exp}}$	B^{calc} (MHz)	$B_{\text{dir}}^{\text{calc}}$
1	44.4(2)	<i>c</i> -axis	44.5(2)	<i>c</i> -axis
1'	34.2(2)	<i>c</i> -axis	34.2(2)	<i>c</i> -axis

D. ZF- μSR measurements for YMn_2O_5

In the case of ZF- μSR for YMn_2O_5 , muon spin precession signals are clearly observed at 32 K (in the CM phase) with $\mathbf{P}_{\mu}||c$ and $\mathbf{P}_{\mu}||a$, as shown in Fig. 4 (a). The FFTs of the spectra shown in Fig. 4 (b) show single and two well-defined peaks for $\mathbf{P}_{\mu}||c$ and $\mathbf{P}_{\mu}||a$, respectively. The corresponding frequencies obtained by curve fitting (B^{exp}) are summarized in Table II. Site1 is predicted to divide into four inequivalent sites because of the magnetic symmetry [shown in Fig. 4 (c)], which we refer to as Site1_{*i*}⁽ⁱ⁾ ($i = 1, 2$). We first calculated \mathbf{B}_{loc} at these sites by assuming that the magnetic moments appear only at the Mn sites in the CM phase obtained by neutron scattering experiments [26]. The calculated magnitude and direction of \mathbf{B}_{loc} are shown in Table II as $B^{\text{calc},\text{Mn}}$ and $B_{\text{dir}}^{\text{calc},\text{Mn}}$, respectively. These magnitudes differ substantially from the experimental values, though their directions are consistent. We next considered the possibility that the magnetic moments appear at the O2 site with their directions parallel to a local magnetic field generated by the neighboring Mn moments, which would be reasonable because the O spin polarization is induced by the Mn magnetic order. The presumed magnetic structure for the O2 sites is shown in Fig. 4 (c). We found excellent agreement between the calculated values for \mathbf{B}_{loc} and those deduced experimentally when the O2 moment size was assumed to be $\sim 0.1 \mu_{\text{B}}$. These results are summarized in Table II as $B^{\text{calc},\text{Mn},\text{O}}$ and $B_{\text{dir}}^{\text{calc},\text{Mn},\text{O}}$. We also calculated the azimuthal angle dependence of resonant intensity at the O *K*-edge for this O2 magnetic structure by using the resonant magnetic scattering amplitude [27], which is shown as the red curve in Fig. 1 (b). The reasonable agreement with experimental observations strongly supports the appearance of magnetic moments at the O2 site inferred from the present μSR measurements.

We also observed muon spin precession signals at 10 K (in the LT-ICM phase) as shown

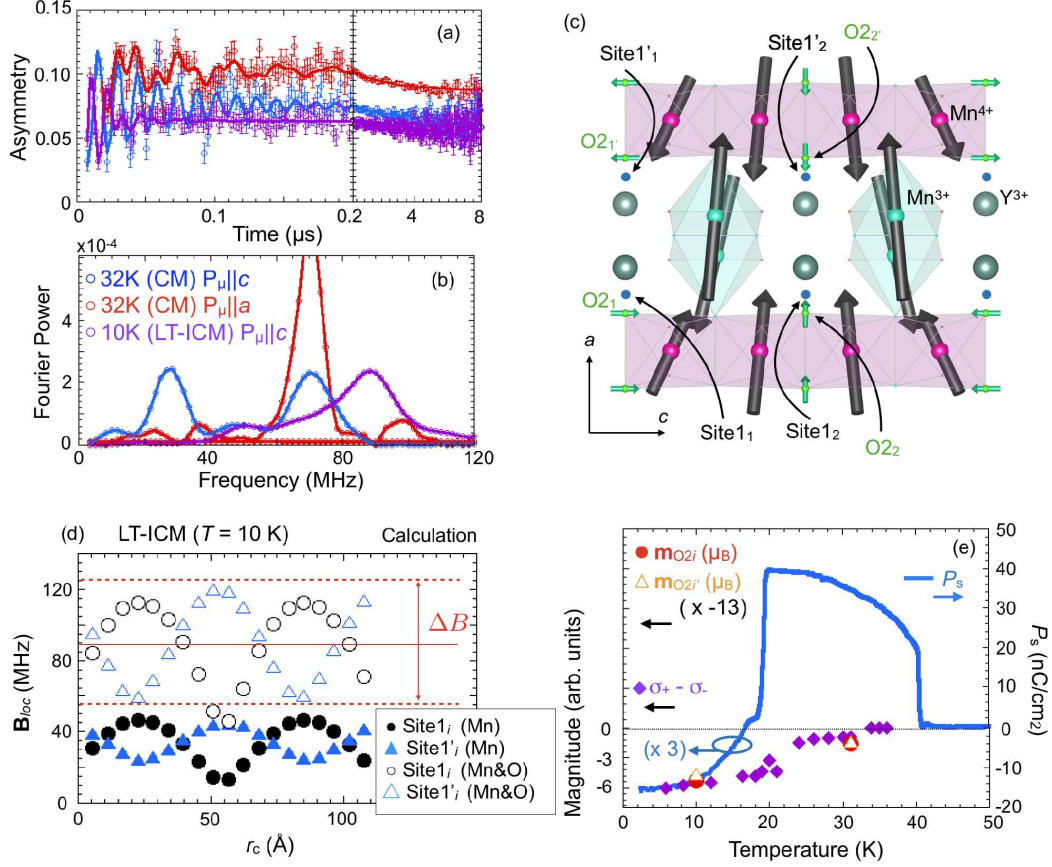


FIG. 4. (Color online). (a) Time spectra and (b) FFT spectra of ZF- μ SR for YMn_2O_5 at 32 K and 10 K. (c) Magnetic structure of Mn and O2 ions in the CM phase of YMn_2O_5 projected onto the ac plane. Black and green arrows represent the magnetic moments of Mn and O2 ions, respectively. The magnitude of magnetic moments at O2 sites is exaggerated for clarity. Filled blue circles represent muon stopping sites $\text{Site1}_i^{(\prime)}$ ($i = 1, 2$). (d) Calculation of B_{loc} at $\text{Site1}_i^{(\prime)}$ for $T = 10$ K. Filled circles (triangles) represent calculated values at $\text{Site1}_i^{(\prime)}$ with only Mn magnetic moments. Open circles and triangles represent calculated values with Mn and O magnetic moments. The data are plotted over different chemical unit cells along the c -axis. The line represents the magnitude of B_{loc} (~ 88.9 MHz), and dashed lines represent the distribution width $\Delta B \sim 70$ MHz. (e) Temperature dependence of the amplitude of the oxygen magnetic moments at O2_i and $\text{O2}_{i'}$ sites (\mathbf{m}_{O2_i} and $\mathbf{m}_{\text{O2}_{i'}}$), $\sigma_+ - \sigma_-$, and the electric polarization (P_s). The $\sigma_+ - \sigma_-$ data are taken from Ref. [18]. The values of P_s corresponding to temperatures below 18 K, \mathbf{m}_{O2_i} , and $\mathbf{m}_{\text{O2}_{i'}}$ are exaggerated for clarity.

in Fig. 4 (a). The time spectrum was analyzed by curve fitting [25], and well reproduces

the experimental results for a single component with frequency $\omega/2\pi = 88.9(1.0)$ (MHz) and relaxation rate $\lambda = 30(10)$ (μs^{-1}). This large relaxation rate is attributed to a wide distribution of \mathbf{B}_{loc} resulting from the incommensurate magnetic structure. To estimate the distribution width of \mathbf{B}_{loc} , we assumed that \mathbf{B}_{loc} follows an isotropic Gaussian distribution,

$$f(B_{\text{loc}}) \propto \exp\left(-\frac{|\mathbf{B}_{\text{loc}}|^2}{2\delta^2}\right), \quad (4)$$

where δ is the dispersion of \mathbf{B}_{loc} . Provided that the \mathbf{B}_{loc} is quasi-static in the time scale of μSR , δ corresponds to the relaxation rate ($\delta \sim \lambda$). This relationship enables us to estimate the full-width at half-maximum of $f(B_{\text{loc}})$ as $\Delta B = 2\sqrt{2\log 2} \cdot \lambda \simeq 70$ MHz, which is comparable to the width of the FFT spectrum at 10 K in Fig. 4 (b). We calculated \mathbf{B}_{loc} at Site1⁽ⁱ⁾ in the incommensurate magnetic structure reported in Ref. [17]. In this magnetic structure, \mathbf{B}_{loc} at Site1⁽ⁱ⁾ varies along the a - and c -axes. The filled symbols in Fig. 4 (d) represent the calculated values of \mathbf{B}_{loc} at Site1_{*i*}⁽ⁱ⁾ ($i = 1 \sim 20$) along the c -axis. The mean and dispersion are considerably smaller than the experimental values, which is common to the case of the CM phase. This result led us to presume that the spin polarization at the O2 sites persists in the LT-ICM phase. The \mathbf{B}_{loc} calculated under the assumption that $0.40(1)$ μ_{B} and $0.36(1)$ μ_{B} at the O2_{*i*} and O2_{*i*'} sites parallel to the local magnetic field at each site is represented by open symbols in Fig. 4 (d); these results are in reasonable agreement with those obtained experimentally.

Wakimoto *et al.* reported in a recent polarized neutron scattering study that the magnitude of vector spin chiral components ($\mathbf{S}_i \times \mathbf{S}_j$) increases in the LT-ICM phase [18]. Figure 4 (e) shows the thermal evolution of the difference in neutron cross section between scattered spin up (σ_+) and down (σ_-) neutrons, which is in proportion to the component of $(\mathbf{S}_i \times \mathbf{S}_j)$, indicating that the spin cycloidal structure of Mn^{4+} develops with decreasing temperature (see Ref. [18] for details). The temperature dependence of the electric polarization is also plotted in Fig. 4 (e) for comparison. For YMn_2O_5 , the electric polarization in the LT-ICM phase is assumed to be mainly driven by the cycloidal spin chains of Mn^{4+} via the SC mechanism, in which spin vector chirality plays a key role. Figure 4 (e) also shows the thermal evolution of spin polarization at O2 sites, as obtained in the present study. On the basis of these data, we concluded that the amplitude of spin polarization at O2 sites increases in the LT-ICM phase with the $(\mathbf{S}_i \times \mathbf{S}_j)$ components. Xiang *et al.* have indicated theoretically for the spiral magnet LiCuVO_4 that spin-orbit (SO) coupling on the Cu sites drives the

TABLE II. Magnitude and direction of local magnetic field (B_{loc}) at Site1 $_i^{(i)}$ ($i = 1,2$) at $T = 32$ K in the CM phase of YMn_2O_5 , as obtained from ZF- μ SR experiments and calculations. $B^{\text{calc,Mn}}$ and $B^{\text{calc,Mn,O}}$ represent the local magnetic field calculated for the Mn and O magnetic structures shown in Fig. 4 (c) assuming zero and finite O magnetic moments, respectively. The direction of B_{loc} at Site1 $_2$ and Site1 $_2'$ is tilted by $\sim 10^\circ$ from the a -axis. The magnitude is represented by the corresponding muon spin precession frequency ($\gamma_\mu B_{\text{loc}}/2\pi$).

Site	B^{exp} (MHz)	$B_{\text{dir}}^{\text{exp}}$	$B^{\text{calc,Mn}}$ (MHz)	$B_{\text{dir}}^{\text{calc,Mn}}$	$B^{\text{calc,Mn,O}}$ (MHz)	$B_{\text{dir}}^{\text{calc,Mn,O}}$
1 $_1$	70.3(4)	c -axis	54(1)	c -axis	70(1)	c -axis
1 $_2$	70.0(5)	a -axis	39(1)	$\sim a$ -axis	70(2)	$\sim a$ -axis
1 $_1'$	27.4(5)	c -axis	41(1)	c -axis	27(1)	c -axis
1 $_2'$	70.3(4)	a -axis	37(1)	$\sim a$ -axis	70(2)	$\sim a$ -axis

asymmetric distribution of electron density mainly around the O atoms [28]. Thus, given that the spin cycloid chain of Mn^{4+} is formed via O2 ions (see Fig. 4 (c)), our results strongly suggest that the SC mechanism is responsible for the imbalance of the charge transfer from the O2 to the Mn^{4+} ions via the p - d hybridization state induced by SO coupling on the Mn sites, thus leading to the local electric and spin polarization of O2 sites in YMn_2O_5 .

Meanwhile, SmMn_2O_5 exhibits a perfect collinear magnetic structure in the CM phase, which has no spin vector chiral component, suggesting the absence of charge transfer between O2 and Mn^{4+} ions in this compound. In fact, no evidence was found in the present study for spin polarization of O2 ions in the CM phase. Thus, we concluded that ionic displacement via the ES model is the main origin of the ferroelectricity in SmMn_2O_5 .

IV. SUMMARY

We successfully observed spin polarization of O2 ions in the multiferroic phase of YMn_2O_5 via the synergetic use of RSXS and μ SR techniques. The amplitude of O spin polarization shows a remarkable increase in the LT-ICM phase in proportion to the vector spin chiral components, implying that the "spin current" model is the most likely scenario for the electronic displacements that result in ferroelectricity with a spin cycloidal structure in multiferroic

materials. The present study thus leads to further understanding of electromagnetic coupling in multiferroic materials and advances the development of multiferroic device applications.

V. ACKNOWLEDGEMENT

We would like to express our thanks to the TRIUMF staff for their technical support during the μ SR experiments and to H. Lee for his assistance with the DFT calculations. This study was supported by the KAKENHI program for Scientific Research (A) (JP15H02038, JP17K05130) and (B) (24340064), Challenging Exploratory Research (2365409), Dynamic Alliance for Open Innovation Bridging Human, Environment and Materials, and Condensed Matter Research Center, IMSS, KEK. This work was performed with the approval of the Photon Factory Program Advisory Committee (Proposals No. 2017G549, No. 2017PF-BL-19B, and No. 2019PF-22).

* yuta.ishii.c2@tohoku.ac.jp; Present address: Department of Physics, Tohoku University, Sendai, Miyagi 980-8578, Japan.

- [1] See, for example, Y. Tokura, S. Seki, and N. Nagaosa, *Rep. Prog. Phys.* **77**, 076501 (2014).
- [2] H. Katsura, N. Nagaosa, and A. V. Balatsky, *Phys. Rev. Lett.* **95**, 057205 (2005).
- [3] Y. Yamasaki, H. Sagayama, T. Goto, M. Matsuura, K. Hirota, T. Arima, and Y. Tokura, *Phys. Rev. Lett.* **98**, 147204 (2007).
- [4] B. Lorenz, Y.-Q. Wang, and C.-W. Chu, *Phys. Rev. B* **76**, 104405 (2007).
- [5] A. S. Moskvin and R. V. Pisarev, *Phys. Rev. B* **77**, 060102(R) (2008).
- [6] A. S. Moskvin and S.-L. Drechsler, *Phys. Rev. B* **78**, 024102 (2008).
- [7] T. A. W. Beale, S. B. Wilkins, R. D. Johnson, S. R. Bland, Y. Joly, T. R. Forrest, D. F. McMorrow, F. Yakhou, D. Prabhakaran, A. T. Boothroyd, and P. D. Hatton, *Phys. Rev. Lett.* **105**, 087203 (2010).
- [8] S. Partzsch, S. B. Wilkins, J. P. Hill, E. Schierle, E. Weschke, D. Souptel, B. Büchner, and J. Geck, *Phys. Rev. Lett.* **107**, 057201 (2011).
- [9] R. A. de Souza, U. Staub, V. Scagnoli, M. Garganourakis, Y. Bodenthin, S.-W. Huang, M. García-Fernández, S. Ji, S.-H. Lee, S. Park, and S.-W. Cheong, *Phys. Rev. B* **84**, 104416

- (2011).
- [10] S. W. Huang, J. M. Lee, H.-T. Jeng, Y.C. Shao, L. A. Wray, J. M. Chen, R. Qiao, W. L. Yang, Y. Cao, J.-Y Lin, R. W. Schoenlein, and Y.-D. Chuang, Phys. Rev. B **94**, 035145 (2016).
- [11] Y. Ishii, S. Horio, H. Yamamoto, Y. Noda, H. Nakao, Y. Murakami, and H. Kimura, Phys. Rev. B **98**, 174428 (2018).
- [12] Y. Ishii, Y. Murakoshi, N. Sato, Y. Noda, T. Honda, H. Nakao, Y. Murakami, and H. Kimura, Phys. Rev. B **100**, 104416 (2019).
- [13] I. Kagomiya, H. Kimura, Y. Noda, and K. Kohn, J. Phys. Soc. Jpn. 70 (Suppl. A), **145** (2001).
- [14] Y. Noda, H. Kimura, M. Fukunaga, S. Kobayashi, I. Kagomiya, and K. Kohn, J. Phys.: Condens. Matter **20**, 434206 (2008).
- [15] Y. Ishii, S. Horio, M. Mitarashi, T. Sakakura, M. Fukunaga, Y. Noda, T. Honda, H. Nakao, Y. Murakami, and H. Kimura, Phys. Rev. B **93**, 064415 (2016).
- [16] H. Kimura, S. Kobayashi, Y. Fukuda, T. Osawa, Y. Kamada, Y. Noda, I. Kagomiya, and K. Kohn, J. Phys. Soc. Japan **76**, 074706 (2007).
- [17] J.-H. Kim, S.-H. Lee, S. I. Park, M. Kenzelmann, A. B. Harris, J. Schefer, J.-H. Chung, C. F. Majkrzak, M. Takeda, S. Wakimoto, S. Y. Park, S.-W. Cheong, M. Matsuda, H. Kimura, Y. Noda, and K. Kakurai, Phys. Rev. B **78**, 245115 (2008).
- [18] S. Wakimoto, H. Kimura, Y. Sakamoto, M. Fukunaga, Y. Noda, M. Takeda, and K. Kakurai, Phys. Rev. B **88**, 140403(R) (2013).
- [19] G. Yahia, F. Damay, S. Chattopadhyay, V. Balédent, W. Peng, E. Elkaim, M. Whitaker, M. Greenblatt, M.-B. Lepetit, and P. Foury-Leylekian, Phys. Rev. B **95**, 184112 (2017).
- [20] B. M. Wanklyn, J. Mater. Sci. **7**, 813 (1972).
- [21] H. Nakao, Y. Yamasaki, J. Okamoto, T. Sudayama, Y. Takahashi, K. Kobayashi, R. Kumai, and Y. Murakami, J. Phys.: Conf. Ser. **502** 012015 (2014).
- [22] G. Kresse and J. Hafner, Phys. Rev. B **47**, 558 (1993);<http://www.vasp.at>.
- [23] Kojima, K. M., *et al.*, Phys. Rev. B **70**, 094402 (2004).
- [24] Tyson, T. A., Deleon, M., Yoong, S., & Cheong, S.-W., Phys. Rev. B **75**, 174413 (2007).
- [25] We analyzed the time spectrum data using the following equations: $A(t) = \sum_{i=1}^m A_i \cos(\omega_i t + \phi) \exp(-\lambda_i t) + C$ for the CM phase and $A(t) = \sum_{i=1}^m A_i J_0(\omega_i t) \exp(-\lambda_i t) + C$ for the ICM phase, where A_i is the partial asymmetry, ω_i is the muon spin precession frequency, ϕ is the initial phase of precession, λ_i is the transverse relaxation rate, C is a constant component,

and $J_0(x)$ is the Bessel function.

[26] Y. Noda, private communication.

[27] J. P. Hill and D. F. McMorrow, *Acta Crystallogr. Sect. A* **52**, 236 (1996).

[28] H. J. Xiang and M.-H. Whangbo, *Phys. Rev. Lett.* **99**, 257203 (2007).